Evaluating trapped lee-wave characteristics over the UK and Ireland in convection-permitting model forecasts using satellite imagery

Article

Published Version

It is advisable to refer to the publisher's version if you intend to cite from the work. See [Guidance on citing](#).

To link to this article DOI: http://dx.doi.org/10.1002/qj.4921

Publisher: Royal Meteorological Society

www.reading.ac.uk/centaur

CentAUR

Central Archive at the University of Reading

Reading's research outputs online

Evaluating trapped lee-wave characteristics over the UK and Ireland in convection-permitting model forecasts using satellite imagery

Hette G. Houtman[1] | Miguel A. C. Teixeira[2] | Suzanne L. Gray[1] |
Peter Sheridan[3] | Simon Vosper[3]

[1]Department of Meteorology, University of Reading, Reading, UK

[2]CEFT/FEUP, Universidade do Porto, Porto, Portugal

[3]Met Office, Exeter, UK

Correspondence
Hette G. Houtman, Department of Meteorology, University of Reading, Reading, UK.
Email: h.g.houtman@pgr.reading.ac.uk

Abstract

Trapped lee waves exert frictional forces on the atmosphere which, due to the small scale of the orography that causes the waves, must be parametrised in coarser-resolution weather and climate models. Because of the scarcity of in situ observations, numerical model data have been used in previous climatological studies of trapped lee waves, which necessitates model evaluation. While the occurrence of trapped lee waves in models has been evaluated in a systematic manner before, their characteristics have not. To this end, the wavelength and orientation of trapped lee waves in the (UK) Met Office's convective-scale variable-resolution model (UKV) are validated against geostationary satellite imagery for the year 2023. The validation is performed using a newly developed wavelet transform technique for the objective estimation of wavelengths and orientations from pre-selected satellite images and corresponding model-derived vertical velocity fields. The model is shown to be skilful in reproducing trapped lee-wave wavelengths, but consistently overestimates them, especially when these wavelengths are below 9 km ($\sim$ six times the model grid spacing). Anisotropy in the satellite's resolution complicates the analysis of wave orientations between the model and the satellite imagery, but they are nonetheless found to be correlated. There is no evidence for a decline in trapped lee-wave production in short-range forecasts and most of the model's skill in wavelength and orientation prediction is retained at a two-day lead time. Overall, the wavelength and orientation of trapped lee waves are generally found to be well-reproduced, which, due to the high sensitivity of trapped lee-wave characteristics to flow parameters, suggests that the UKV provides an accurate representation of the conditions relevant to trapped lee-wave formation. The model may therefore be considered a suitable substitute for observations in climatological studies of trapped lee waves and in the future development of a trapped lee-wave drag parametrisation.

KEYWORDS

model evaluation, satellite imagery, trapped lee waves, wavelet transform

1 | INTRODUCTION

Trapped lee waves are the shortest amongst atmospheric gravity waves and are thus the last to become resolved in numerical weather prediction and climate models, as their resolution improves with time. Studies of the preconditions and characteristics of trapped lee waves in models may be used to help inform future trapped lee-wave drag parametrisations, but little systematic model validation against observations has been performed. In this article, an evaluation of trapped lee-wave characteristics in the Met Office's UK variable-resolution model (UKV) is presented.

Vertically propagating orographic gravity waves have received much attention in recent years because of their role in momentum transport through the atmosphere and their consequent effect on the larger-scale dynamics and climate (Fritts & Alexander, 2003; Nappo, 2012; Xu *et al.*, 2021). Because the orography that generates gravity waves is often of too small scale to be represented properly in numerical weather prediction and climate models, the drag they produce must be parametrised. This parametrisation is commonly done for vertically propagating waves in current models (Kim & Doyle, 2005; Lott & Miller, 1997; McFarlane, & McFarlane and A., N., 1987). In some stably stratified flows, however, gravity waves generated at the surface do not propagate vertically and are instead trapped at low levels in the atmosphere (Scorer, 1949). Such waves (called trapped lee waves) also produce wave drag, despite their non-hydrostatic nature (Bretherton, 1969). Moreover, in recent studies, trapped lee waves have been shown to be capable of producing drag of comparable magnitude to that produced by their vertically propagating, hydrostatic counterparts (Stiperski & Grubišić, 2011; Teixeira *et al.*, 2013b). Trapped lee-wave drag is not currently parametrised in any operational weather forecast or climate models (to the authors' knowledge), owing at least in part to the relative difficulty with which analytic expressions for the wave drag are obtained outside the hydrostatic regime (Teixeira & Argaín, 2022). Steeneveld *et al.* (2008) observed that many numerical weather prediction models contain unphysically high turbulent drag in the boundary layer and suggested that unparametrised terrain drag at low levels is what causes the need for so-called long-tail turbulence schemes. As trapped lee waves commonly form at low levels, their study further motivates the development of a trapped lee-wave drag parametrisation. Although progress has been made in recent years regarding the theory of trapped lee-wave-induced drag (e.g., Teixeira *et al.* (2013a, 2017); Teixeira and Argaín (2022)), to develop a trapped lee-wave drag parametrisation a thorough understanding of their real-life manifestations is also required.

In situ observations of trapped lee waves are scarce, which complicates the climatological study of these waves and their effects. Geostationary satellite measurements provide the only continuous observations of trapped lee waves over longer time periods and therefore provide a potential basis for climatologies. Grubišić and Billings (2008) produced such a satellite-derived climatology of lee waves over the Sierra Nevada in California. They identified trapped lee-wave cloud bands by eye from satellite imagery for October–May (1999–2001) and found wavelengths between 4 and 32 km, with the average being between 10 and 15 km. A limitation of the use of satellite imagery is that only the wavelength and orientation of the waves can be extracted and not, for example, their amplitude, which largely determines the resulting drag; nor can much be inferred about the atmospheric conditions that cause the waves, apart from perhaps the larger-scale, synoptic conditions. In addition, typically only the visible channel of the imaging instrument is of high enough resolution to resolve short-wavelength lee waves, which limits the scope of satellite-based climatologies to daytime occurrences. In contrast, numerical model data, particularly the archived data of operational forecast models of high enough resolution to (partially) resolve trapped lee waves, provide a wealth of information on wave characteristics and the associated atmospheric conditions and are not limited to daytime occurrences. For example, Vosper *et al.* (2013) used three years of archived data from an operational Met Office model to produce a trapped lee-wave climatology over the UK. As such, they were able to make more detailed climatological statements, such as on the effect of incident wind speed and wind turning on lee-wave amplitudes. More recently, Coney *et al.* (2024) used a deep learning technique to develop a model-derived climatology of trapped lee waves and examine the relative importance of different model variables on trapped lee-wave generation. Incident wind speed, the Scorer parameter, and buoyancy frequency were found to be most important and waves were found to be most frequent under westerly flows.

The obvious issue with model-derived climatologies, however, is that models do not necessarily represent reality correctly. Validation of the representation of trapped lee waves in models is therefore desirable. This validation can be performed by comparing model outputs with in situ measurements, as was done in Sheridan *et al.* (2007) and in several field campaigns, such as the Pyrénées Experiment (PYREX) and the Mesocale Alpine Programme (MAP) (Georgelin & Lott, 2001; Smith *et al.*, 2007). Alternatively, model outputs may be compared with satellite imagery. In Vosper *et al.* (2013), 97% of trapped lee-wave cases identified in satellite imagery were reproduced in the Three-dimensional

Velocities Over Mountains (3DVOM) model, which was driven by the Met Office's operational global forecast model. This result suggests the global model has high skill in capturing the environmental conditions that produce trapped lee waves. It is unclear, however, whether the model's representation of the conditions is accurate enough to predict the characteristics (such as wavelength, orientation, and amplitude) of trapped lee waves correctly, in addition to just their presence. In Vosper *et al.* (2013) and Sheridan *et al.* (2017), some validation of lee-wave characteristics against observations was performed and produced favourable results, but in both studies the evaluation was conducted only in a qualitative manner and only on a few cases.

The aim of this article is to provide a more systematic evaluation of the UKV's representation of trapped lee waves by identifying trapped lee waves in satellite imagery over a one-year period and comparing their wavelength and orientation with those found in the model output. To be able to compare trapped lee-wave characteristics quantitatively and objectively, a new method of lee-wave characterisation involving wavelet transforms was developed. This evaluation of trapped lee-wave characteristics in the model provides a more detailed (albeit indirect) assessment of the preconditions for trapped lee waves in the model than has been obtained before, which is useful for the following reasons. Firstly, it will help further to determine whether the UKV is a suitable substitute for observations in establishing the preconditions for trapped lee waves and, if so, what the potential caveats are. Secondly, it will inform the development of a future trapped lee-wave drag parametrisation, as any shortcomings of the model in representing the relevant conditions must be taken into account in the parametrisation scheme. Note that the use of satellite imagery limits this article to an assessment of wavelengths and orientations, and places an evaluation of wave amplitudes outside its scope.

The remainder of this article is structured as follows. The data used in this study are described in Section 2, followed by the wavelet transform method developed to characterise lee waves objectively in Section 3. The results of the comparison between the imagery and model output are presented in Section 4. Finally, Section 5 contains the summary and conclusions.

2 | DATA

The model data analysed here are the hourly analyses and forecasts of the vertical velocity field (w) in the operational UKV for the year 2023. The UKV domain covers the UK and Ireland, and derives its lateral boundary conditions from the global configuration of the Met Office Unified Model (MetUM). The native grid of the UKV has a variable grid spacing, from 4 km at the boundaries to 1.5 km in the inner domain (Tang *et al.*, 2013). Only data from the inner domain are considered in this study. Within the inner domain, the model resolution is high enough for lee waves to be resolved, at least in some cases (Sheridan *et al.*, 2017). The vertical velocity field is, arguably, not the field most comparable with satellite imagery. Instead, one could choose the top-of-atmosphere (TOA) radiative flux field or simulate synthetic satellite imagery from the model fields using, for example, Radiative Transfer for TIROS Operational Vertical Sounder (RRTOV: (Saunders *et al.*, 2018)). However, it was found that these alternative data contain weaker trapped lee-wave signals, presumably because they are susceptible to errors in more than one prognostic model field. For example, the model may predict lee-wave activity correctly but, if it underestimates the moisture content, this might not result in a detectable signal in the cloud cover field. Because the only wave characteristics that can be retrieved from satellite imagery are wavelength and orientation, which can be assumed to be the same in all model variables affected by the waves, it suffices to analyse a model field with a clear signal. Thus, in this work the w field was used, as contributions to it by phenomena other than gravity waves are typically small (with perhaps the exception of convection, which the UKV model represents explicitly). The w field was analysed at the 700-hPa level (following Vosper *et al.* (2013) and Coney *et al.* (2023)), as well as 600 hPa and 800 hPa. The sensitivity of the results to the choice of analysis level is discussed in Section 4.1.

The UKV data were compared with imagery obtained from the Spinning Enhanced Visible and InfraRed Imager (SEVIRI) instrument aboard the geostationary *Meteosat Second Generation* satellite (Schmetz *et al.*, 2002). The satellite provides high-resolution (1 km × 1 km at nadir) measurements of the TOA reflectance in the high-resolution visible channel (HRV, 0.4–1.1 μm). This instrument was chosen over those on polar-orbiting satellites due to its higher sampling rate (every 15 minutes, as opposed to roughly once a day), which increased the number of detectable lee-wave cases. Although polar-orbiting satellites tend to provide higher resolution imagery, the resolution of SEVIRI's HRV channel is higher than that of the model considered in this work and was therefore not considered a limiting factor (although this assumption is revisited in Section 4.2). The use of visible imagery limits the scope of this work to daytime occurrences of trapped lee waves. Infrared imagery would allow for night-time detection of trapped lee waves but, at one-third of the resolution of the HRV imagery (3 km), would limit the analysis of smaller wavelengths severely. For comparison, both the satellite imagery and the UKV data were regridded onto the same latitude–longitude grid with a grid spacing of approximately 1 km before analysis.

3 | METHODS

The sections below describe the methods developed for this study: firstly, the method for the identification of trapped lee waves from satellite imagery and, secondly, the method for the estimation of trapped lee-wave characteristics.

3.1 | Identification of trapped lee waves from satellite imagery

Occurrences of trapped lee waves in the HRV imagery were identified by eye as follows. For each day, starting with the earliest image that daylight allowed, any cloud bands in the clouds were identified. Using imagery from previous and subsequent time steps, it was determined whether the cloud bands were (1) orientated roughly perpendicular to the wind direction (inferred from the movement of cloud features), in which case they were more likely to be the result of lee waves and not of other phenomena such as convective rolls (which are aligned approximately parallel to the wind), and (2) stationary. If both conditions were fulfilled, then the date and the region(s) of occurrence were noted. The different regions considered are displayed in Figure 1. Predetermining the regions of occurrence reduced significantly both the computational expense of later analysis (as the area analysed could be made smaller) and the risk of contamination by non-trapped lee-wave signals in the analysed data. For each date and region, the

time of day selected for later analysis was chosen to be the whole hour (to allow for comparison with the hourly outputs of the UKV model) at which the cloud signal was judged to be clearest. Note that this method does not detect all instances of trapped lee waves. Only daytime occurrences can be detected due to the use of visible imagery and, even if waves are present during daytime, conditions simply may not be conducive to the formation of clear cloud patterns: for example, the moisture content may be too low for condensation to occur, the wave amplitude may not be large enough to cause a noticeable difference in cloud reflectance, or cloud formations at higher levels may obscure cloud bands lower down. Risk of human error is also present.

3.2 | Algorithm for estimation of wave characteristics

3.2.1 | Wavelet transforms

The wavelet transform and related techniques (such as the S-transform) have been used extensively in the analysis of gravity waves since their introduction in the 1980s (Nappo, 2012; Torrence & Compo, 1998). Recent examples of the application of wavelet and S-transforms to gravity-wave signals are given by Hindley *et al.* (2015, 2016) and Coney *et al.* (2023). The wavelet transform retains resolution in space (time) as well as in wavenumber (frequency) and is therefore useful for the extraction
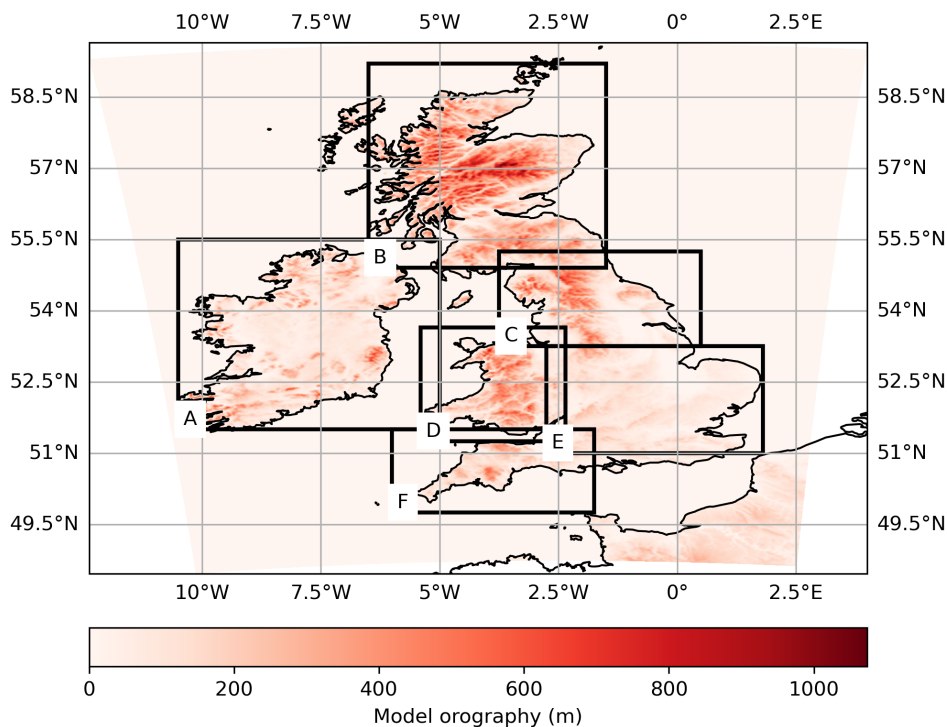

FIGURE 1 The regions used in the pre-selection of satellite imagery and later analysis, shown over the UKV model orography. A: Ireland, B: Scotland, C: North England, D: Wales, E: England, F: Southwest England. [Colour figure can be viewed at wileyonlinelibrary.com]

of the characteristics of gravity waves, which are often localised and intermittent. It may be interpreted as the cross-correlation of a signal, S, with a "wavelet" function, ψ. In two dimensions, this may be expressed as follows:

$$W[S(\mathbf{x})](\mathbf{x}, a, \varphi) = \int_{-\infty}^{\infty} \int_{-\infty}^{\infty} S(\mathbf{x}') \frac{1}{a} \psi^* \left(\mathbf{R}_\varphi \frac{\mathbf{x}' - \mathbf{x}}{a} \right) d\mathbf{x}', \tag{1}$$

in which ψ^* denotes the complex conjugate of the wavelet function and $\mathbf{x}'$ is a dummy vector. The prevalence of different length-scales and orientations in S can then be determined by scaling $\psi(\mathbf{x})$ (the "mother wavelet") by the spatial scale parameter a and rotating it anticlockwise by an angle φ:

$$\mathbf{R}_\varphi = \begin{pmatrix} \cos\varphi & -\sin\varphi \\ \sin\varphi & \cos\varphi \end{pmatrix}. \tag{2}$$

In this work, we choose the complex Morlet wavelet, a complex wave with Gaussian amplitude:

$$\psi(\mathbf{x}) = \frac{1}{\sqrt{\pi}} \exp(i\mathbf{k}_0 \cdot \mathbf{x}) \exp\left(-\frac{|\mathbf{x}|^2}{2} \right), \tag{3}$$

with $\mathbf{k}_0 = (6, 0)$ to satisfy the admissibility condition of the wavelet transform (Wang & Lu, 2010). Because $\mathbf{k}_0$ is fixed, it is the scale parameter a that specifies the wavenumber of the wavelet. The scale parameter can be related to an equivalent Fourier wavelength λ. For the Morlet wavelet (Meyers et al., 1993),

$$\lambda = \frac{4\pi a}{|\mathbf{k}_0| + \sqrt{2 + |\mathbf{k}_0|^2}} \approx 1.03a. \tag{4}$$

This means the wavelet power spectrum can be defined in terms of λ and ϑ (Chen & Chu, 2017):

$$P(\mathbf{x}, \lambda, \vartheta) = \frac{|W|^2}{a^2}, \tag{5}$$

where ϑ is now the clockwise angle that the wavelet wavevector makes from north.

3.2.2 | Implementation

The main difficulty in extracting lee-wave wavevectors from the data using wavelet transforms is in distinguishing between true trapped lee-wave signals and other non-trapped lee-wave signals. This is especially true for satellite imagery, which often contains many different cloud formations and is thus noisy compared with the model-derived vertical velocities. Although the prevalence of non-trapped lee-wave signals in the satellite imagery has been limited by considering only images in which

lee waves have already been identified by eye, some extra criteria need to be placed upon the wavelet transforms to ensure only trapped lee-wave signals are extracted. Attempts to enhance trapped lee-wave signals in satellite imagery through imaging processing techniques, such as thresholding and histogram equalisation, produced mixed results, and thus for simplicity such techniques were not used. The following procedure was used to estimate trapped lee-wave characteristics, in both the satellite imagery and the UKV data.

1. Calculate $P(\mathbf{x}, \lambda, \vartheta)$ at 5° angle intervals in the range $[0°, 175°]$ and at 50 logarithmically spaced values of λ between 3 and 35 km. This range of wavelengths encompasses that of American Meteorological Society (2024), but with the lower limit reduced from 5 km, as some cases of trapped lee waves in the satellite imagery were found to have shorter wavelengths.

2. At each pixel, identify the wavelength and orientation of the most dominant wave signal, that is, the wavevector (λ, ϑ) at the local spectral peak of P, for which the following holds.

   a. $P(\lambda, \vartheta)/\sigma^2 \geq 10^{-2}$, where σ^2 is the variance of the image. This threshold value is somewhat arbitrary, but ensures the signal is sufficiently strong compared with the image's variance. This threshold helps exclude spurious signals, such as variations in land-surface reflectance in the case of satellite data.

   b. The edges of the image lie outside the wavelet cone of influence, defined as a distance of $\sqrt{2}a$ $(\approx \sqrt{2}\lambda)$ from the pixel in question (Torrence & Compo, 1998). Note that in some pixels there might not be any wavevector that satisfies these criteria. If there is a strong signal sufficiently removed from the edges of the image, then we require the following.

   c. $|\Delta| \leq 50°$, where Δ is the difference between ϑ and the UKV-derived wind direction in the pixel at the specified pressure level. While such oblique trapped lee waves are possible, they are rare, and by excluding all such oblique signals we filter out unwanted signals, such as convective roll cloud bands. This threshold for $|\Delta|$ is justified in Section 4.2.

   Note that overlapping waves with different orientations or wavelengths are neglected by this algorithm, as only one combination of (λ, ϑ) may be chosen per pixel.

3. Bin the selected wavevectors across the image in a histogram. As each pixel covers a roughly equal area, this is equivalent to calculating the area covered by trapped lee waves of different wavevectors.

4. To determine most prevalent wave signals, smooth the histogram with a Gaussian filter (with a σ of roughly 0.05 in $\ln\lambda$ and 5° in ϑ) and find the local maxima.

5. Finally, to distinguish trapped lee waves from other cloud features, such as the edges of extended cloud cover, use the fact that trapped lee waves are by nature repeating and require these local maxima to be larger than λ^2, that is, require the area over which the wavevector is spread to be large compared with its wavelength.

Figure 2 serves to illustrate the working of this algorithm when applied to satellite imagery. In Figure 2a, the normalised power spectrum is used to distinguish regions that might contain trapped lee waves from their surroundings (step 2 above). Because the variation in the measured TOA reflectance varies greatly between cases, it is impossible to set a single threshold on the power spectrum that differentiates trapped lee waves from their surroundings perfectly in all cases, even when normalising by the variance (step 2a). To prevent too many non-trapped lee-wave signals from contaminating the further analysis, an arguably high value of 10^{-2} was chosen for the power-spectrum threshold, at the cost of neglecting some true trapped lee-wave signals. This effect is exemplified in Figure 2, where large regions visibly containing lee waves do not rise above the threshold and are thus excluded, but, in return, there are few non-trapped lee-wave signals entering further analysis (step 3). After smoothing, the local maxima in the histogram are recorded as the detected trapped lee-wave wavevectors for that case (step 4). By requiring that the local maxima are larger than λ^2, some spurious signals that are not repeated sufficiently to be identifiable as trapped lee waves are disregarded, such as the short-wavelength signals detected near the left edge of the image.

4 | RESULTS

Using the methodology described in Section 3.1, 463 cases of trapped lee waves, spread across 206 days, were identified by eye in the 2023 satellite imagery. The number of days with identified trapped lee waves ranged from 10 to 28 per month. We reproduce the findings in Vosper et al. (2013) and Coney et al. (2024) that lee waves are most prevalent over Scotland and least common over Southwest England (Figure 1), although it must be noted that the sizes of the domains contribute to the respective number
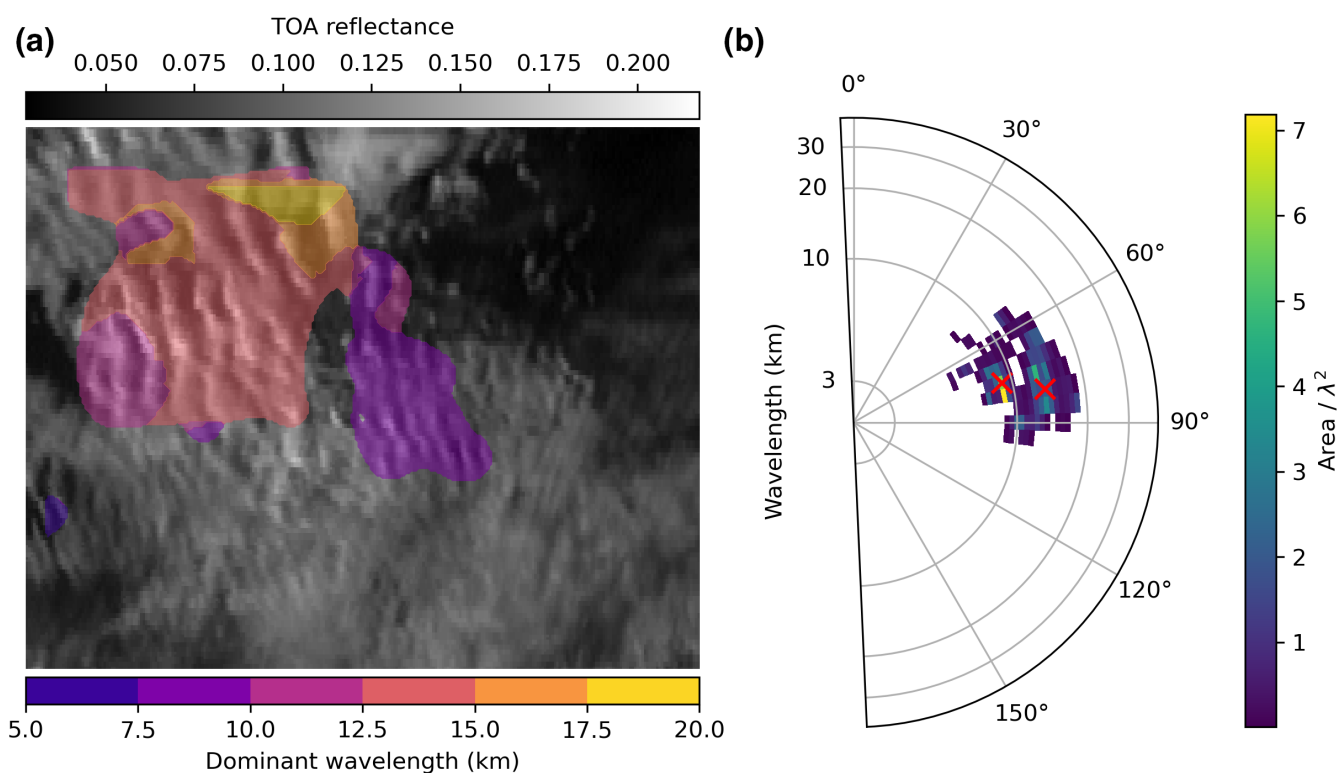

FIGURE 2 (a) TOA reflectance as measured by the SEVIRI instrument in the HRV channel over the North England region on January 29, 2023 at 1500 UTC. Overlaid is the dominant wavelength detected by the algorithm (where max $P/\sigma^2 \geq 10^{-2}$). (b) Histogram of the detected wavelengths and orientations, with histogram counts expressed as area scaled by λ^2. Red crosses indicate the wavevectors selected by the algorithm (i.e., the local maxima larger than λ^2 after smoothing). Of these, only the wavevector covering the largest area is used in the case-by-case comparisons between the UKV and SEVIRI data. [Colour figure can be viewed at wileyonlinelibrary.com]

of occurrences. In 76% of cases (353 out of 463) at least one trapped lee-wave wavevector was detected in the satellite imagery by the algorithm described in Section 3.2. The fact that the algorithm did not detect any wavevectors in roughly a quarter of the images can be attributed to the noisy nature of the satellite imagery and the restrictive criteria set in the algorithm. In the UKV w field, wavevectors were detected in all cases. This true positive rate of 100% is in good agreement with Vosper *et al.* (2013), in which the studied model, also driven by the Met Office's global model, had a 97% true positive rate. Although wave signals are clearer in the model w field than in the satellite imagery, it is possible that, in a small number of cases of non-trapped lee waves, signals produced by the model did enter further analysis. The sections below discuss the detected wave characteristics.

4.1 | Wavelength

Figure 3 displays histograms of the wavelengths detected in the satellite imagery and at different pressure levels in the UKV data, respectively. Since it is unknown at which heights the trapped lee-wave cloud signatures that were analysed in the satellite imagery formed, the UKV w field was analysed at 600- and 800-hPa levels in addition to the 700-hPa level. The fact that most wavevectors are detected at 800 hPa suggests that trapped lee waves are most prevalent at that level in the model. In addition, Figure 3 shows that the shape of the UKV wavelength distribution at this level, being bimodal (peaks at 8 and 12 km) and having a lower frequency of waves at longer wavelengths than the other levels, follows that of the satellite imagery most closely. Therefore, the UKV data were analysed at the 800-hPa level for the remainder of this article and, in algorithm criterion 2c, the detected orientations were compared with the wind direction at that pressure level. Note, though, that the standard deviation in w is highest at 700 hPa, although it does not vary greatly between the pressure levels studied.

The wavelength distributions of the 800-hPa UKV w field and the satellite imagery are qualitatively similar, with that of the UKV shifted towards longer wavelengths. In the satellite imagery, the detected wavelengths cover the range investigated almost entirely (the minimum and maximum are roughly 3 and 30 km, respectively), but the vast majority of wavelengths (94%) are shorter than 15 km and only two are longer than 25 km. This distribution of wavelengths is consistent with that found by Grubišić and Billings (2008). The lower limit of the UKV's resolution is around 6 km (four times the grid spacing), with less than 1% of detected wavelengths being shorter than this. Also, in the model most wavelengths (90%) are shorter than 15 km and only two wavelengths were found to be longer than 25 km. At the upper end of the distribution, the model and satellite data are thus rather similar, unlike at the lower end.

Figure 4 displays a case-by-case comparison of the UKV and satellite-derived wavelengths. Although the algorithm described in Section 3.2 allows for detection of multiple wavevectors per case, for some trapped lee-wave cases significant spatial variations in wavelength and orientation were observed. In these cases, it is not trivial to assign the wavevectors detected in the UKV data to those
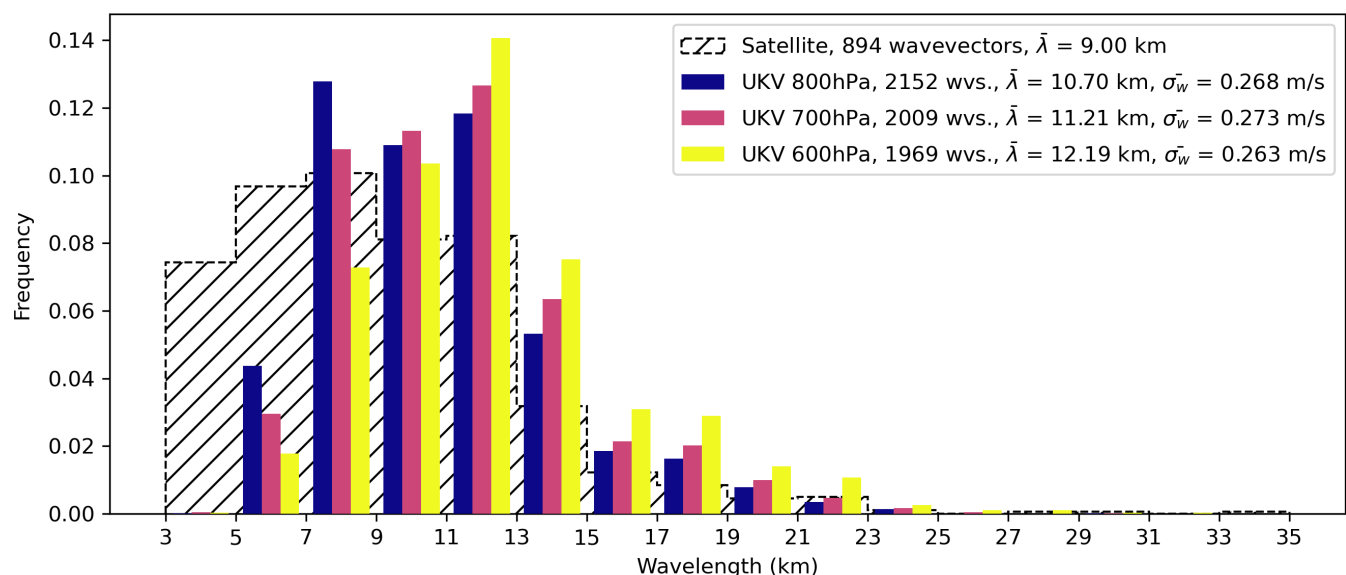

FIGURE 3 Histogram of all model-derived wavelengths at 600, 700, and 800 hPa, compared with those detected in the satellite imagery. [Colour figure can be viewed at wileyonlinelibrary.com]
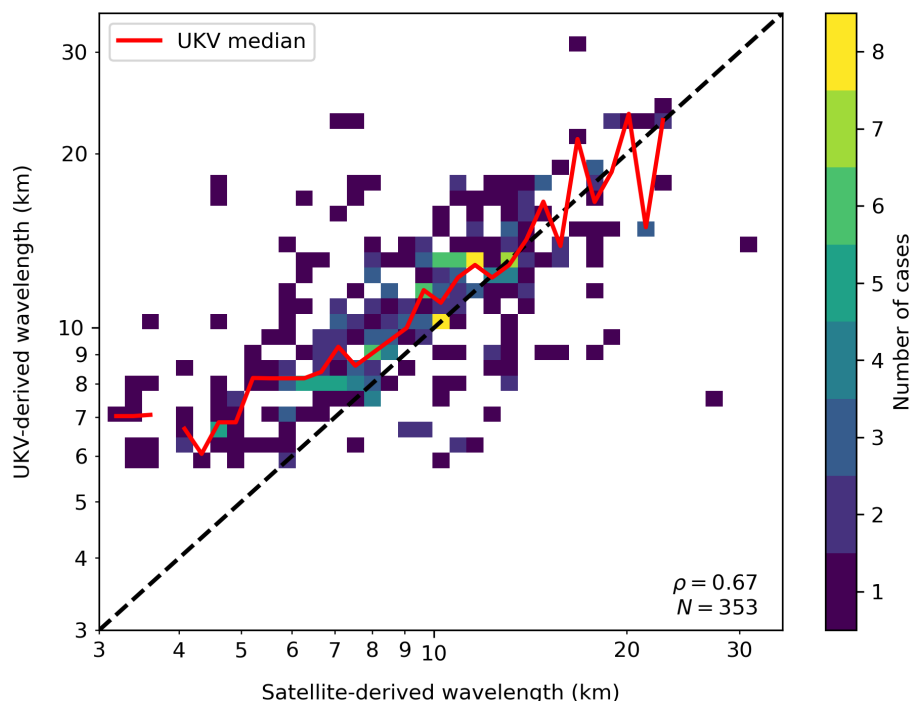
FIGURE 4 2D histogram comparing the wavelengths extracted from the satellite imagery and UKV analyses per case. The red line displays the median of UKV-derived wavelengths as a function of satellite-derived wavelengths. [Colour figure can be viewed at wileyonlinelibrary.com]

detected in the satellite imagery. Therefore, for simplicity, only the most prevalent wavevector (i.e., the largest peak in the right panel of Figure 2) is considered for each case in the following case-by-case comparisons. Note, however, that this choice disregards any spatial variation of the wavevector within the region of analysis and in some cases worsens the apparent agreement between the two data sources. For instance, in Figure 2, the observed wavelength increases sufficiently in the westward direction (Figure 2a) that two representative wavevectors are selected (Figure 2b), with the longer-wavelength one being most prevalent. In a case where, in the model, this spatial variation of the wavevector is captured well but the shorter wavelength waves are slightly more prevalent, a large discrepancy in the case-by-case analysis would result and the model's skill in capturing the spatial variation of the waves would not be apparent.

Despite some amount of scatter, a positive correlation between the wavelengths determined from the model output and satellite data can be identified by eye in Figure 4 (Spearman correlation coefficient $\rho = 0.67$), indicating that the UKV has some skill in producing accurate trapped lee-wave wavelengths. As in Figure 3, though, the UKV-derived wavelengths are generally longer, as most points lie above the identity line. Because of the limited effective resolution of the UKV, an overestimation of wavelengths shorter than about 9 km ($\sim$ six times the grid spacing) would certainly be expected. Indeed, in this comparison, wavelengths shorter than 9 km are overestimated by 46% on average in the UKV. As can be seen from the median of UKV-derived wavelengths asymptoting towards

the identity line, the overestimation of wavelength lessens as the wavelength increases. Due to the low number of cases (35) with wavelengths longer than roughly 15 km, however, it is unclear whether the overestimation disappears completely. At the 700- and 600-hPa levels, the results are qualitatively similar, but with larger scatter ($\rho = 0.59$ and 0.44, respectively, not shown).

4.2 | Orientation

Histograms of the trapped lee-wave orientations detected are shown in Figure 5a. There is a marked difference between the satellite imagery and the UKV (which does not change significantly when analysed at different pressure levels): in the model there is no clear preference towards a single wavevector orientation, while in the satellite imagery there is a clear preference towards roughly 90° from north (with wave crests thus being oriented roughly north–south). In Figure 5b, the orientations are compared case-by-case and the preference in the satellite imagery for east–west orientated wavevectors is reflected in the tilting of the histogram with respect to the identity line. Despite the tilting and the large amount of scatter, a generally positive trend between the satellite and model data can still be identified by eye ($\rho = 0.68$).

Figure 6, which shows 2D histograms of the detected wavevectors for the satellite imagery and the UKV, reveals that the preferred east–west orientation of the satellite-derived wavevectors is stronger at shorter wavelengths. We therefore hypothesise that this bias an
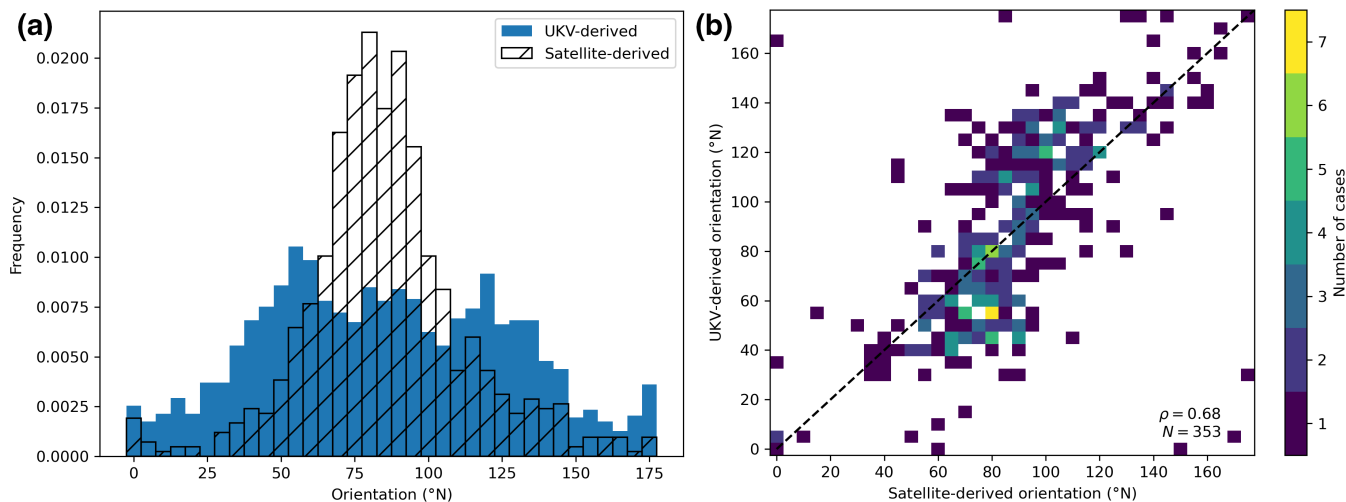
FIGURE 5 (a) Histograms of all UKV-derived and satellite-derived orientations. (b) As in Figure 4, but for wavevector orientations. [Colour figure can be viewed at wileyonlinelibrary.com]
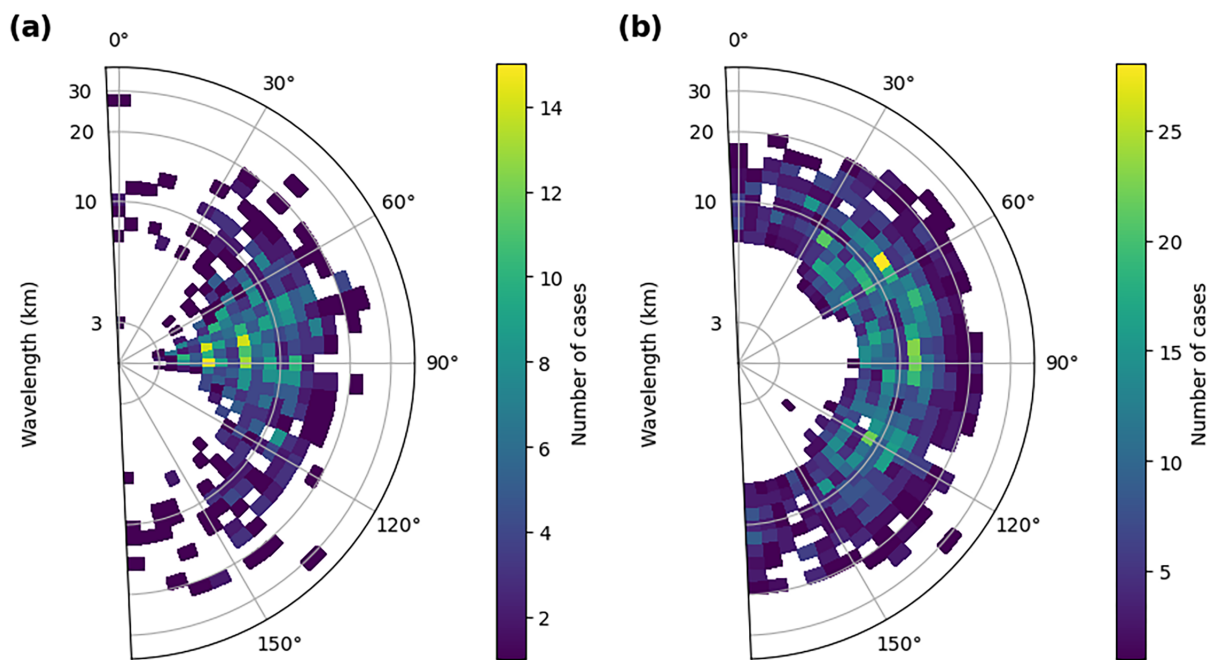

FIGURE 6 2D histograms of all selected wavevectors in (a) the satellite imagery and (b) the UKV. [Colour figure can be viewed at wileyonlinelibrary.com]

artefact of the effective meridional grid spacing of the imaging instrument, which scales with latitude, y, as $1/\cos y$. When viewing the UK and Ireland (centred at roughly 55°N, 5°W), the effective meridional grid spacing of the instrument (which orbits at 0°N, 0°E) is increased by a factor of $1/\cos 55° \approx 1.74$, whereas its effective zonal grid spacing, which scales with longitude as the meridional grid spacing scales with latitude, remains largely unaffected ($\cos(-5°) \approx 1$). This makes short-wavelength waves harder to detect if their wavevector is orientated meridionally.

Figure 7 displays an example case of trapped lee-wave activity over Southwest England that supports this hypothesis. Figure 7a,c,e shows, respectively, the imagery taken by the geostationary SEVIRI instrument, imagery taken by the polar-orbiting *Aqua* Moderate Resolution Imaging Spectroradiometer (MODIS: MODIS Science Team (2017)) instrument, and the UKV 800-hPa vertical velocity analysis. The MODIS instrument has a higher resolution (250 m at nadir) than SEVIRI and, at the time of measurement, was orbiting over the North Sea and therefore had a viewing angle close to 0°. In the highlighted region in Figure 7,
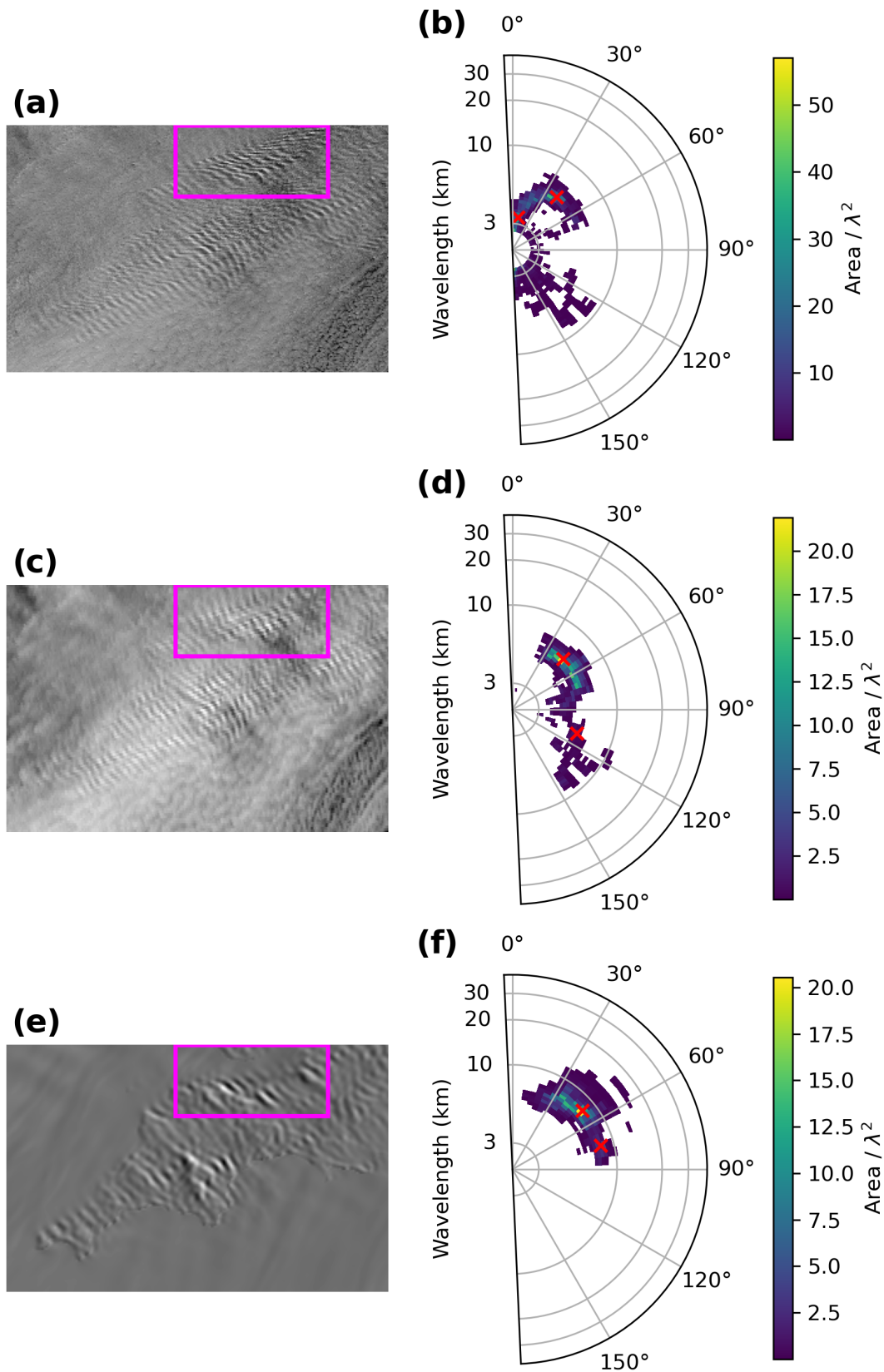
FIGURE 7 Example case of trapped lee-wave activity over Southwest England on December 17, 2023, 1300 UTC. The analysed data and corresponding detected signals are shown for (a,b) MODIS imagery, (c,d) SEVIRI imagery, and (e,f) UKV 800-hPa vertical velocity analysis. The region highlighted in magenta contains waves highly oblique to the wind direction in (a), but not in (c) or (e). Because of the presence of these oblique waves in this example case, the restriction on Δ (criterion 2c) was not applied for these figures. [Colour figure can be viewed at wileyonlinelibrary.com]

the polar-orbiting image contains short-wavelength waves oblique to the wind direction, with the cloud bands being orientated east–west, whereas in the geostationary image and the model data these bands are not present. The output of the algorithm, shown in Figure 7b,d,f, confirms the presence of short-wavelength, meridionally orientated waves in the polar-orbiting image and the absence of any such signals, whether from trapped lee waves or not, in the geostationary image and model data. Furthermore, compared with the polar-orbiting image, we see an increased signal in the geostationary image of waves orientated at around 60° and above, which supports the claim that zonally
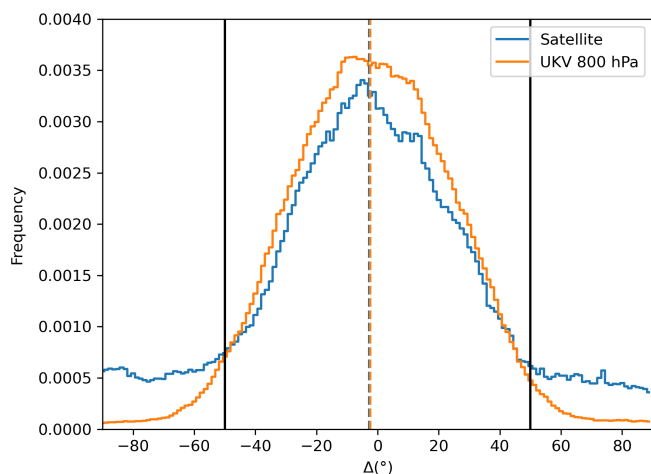
orientated waves appear more dominant in the geostationary imagery.

Figure 8 shows a histogram of the difference between the UKV-derived wind direction at 800 hPa and the wave orientation detected by the wavelet transform algorithm at each selected pixel (i.e., the coloured pixels in Figure 2a). The peak of the distribution has a negative offset (mean $-2.8°$), meaning the waves are generally turned anti-clockwise with respect to the wind direction. This offset increases at lower pressures, which is consistent with the wave orientation remaining constant while the wind at lower levels backs increasingly due to surface friction. The offset between wind direction and wave orientation and its increase with altitude are also present in the UKV (mean of $-2.4°$ at 800 hPa). Beyond around $|\Delta| = 50°$, the UKV-derived and satellite-derived frequencies start to diverge, with the frequency of signals in the satellite imagery remaining approximately constant beyond $|\Delta| = 50°$. This finding suggests that beyond this value the detected signals are increasingly from non-trapped lee-wave sources, since we expect the frequency of trapped lee-wave signals to decay to zero as $|\Delta| \rightarrow 90°$, as is observed in the UKV data. The threshold for $|\Delta|$ in the lee-wave characterisation algorithm was therefore set at 50°.

4.3 | Forecasts

In addition to the model analyses, the algorithm was applied to two- and five-day forecast data, valid at the same pre-selected dates and times. Because UKV forecasts of lead times longer than 12 hours are not issued at every
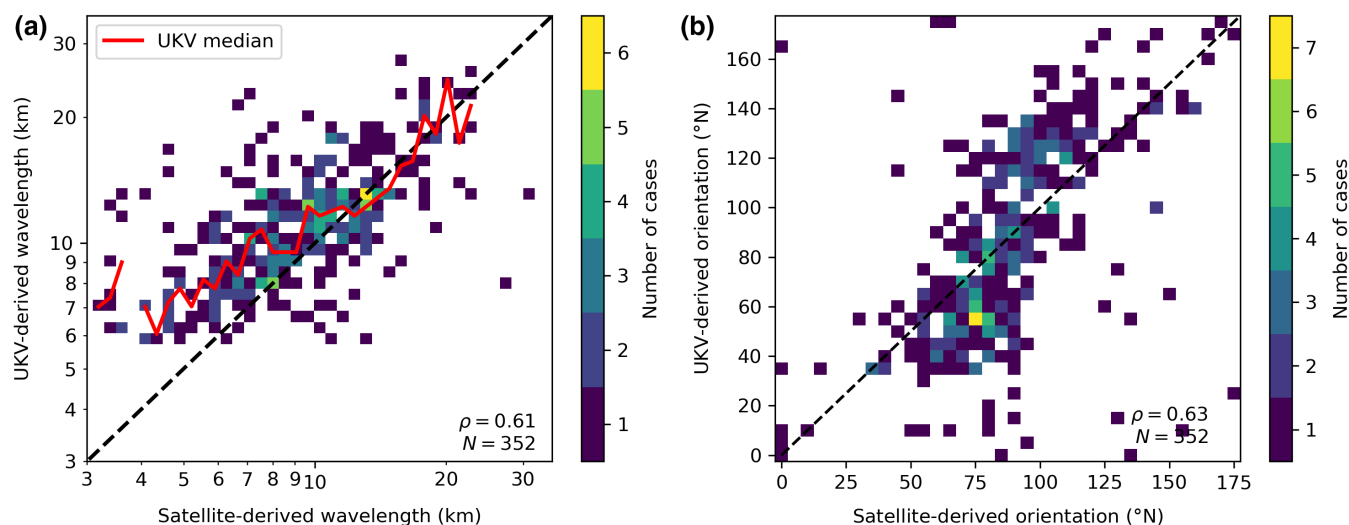

FIGURE 8 The frequency of Δ across all selected pixels in the UKV and satellite data. The dashed vertical lines indicate the mean Δ for both data sources, while the black vertical lines indicate the imposed cut-off at $|\Delta| = 50°$. [Colour figure can be viewed at wileyonlinelibrary.com]

FIGURE 9 Histograms comparing (a) wavelengths and (b) orientations extracted from the satellite imagery and two-day lead time UKV forecasts, per case. The red line displays the median of UKV-derived wavelengths as a function of satellite-derived wavelengths. [Colour figure can be viewed at wileyonlinelibrary.com]
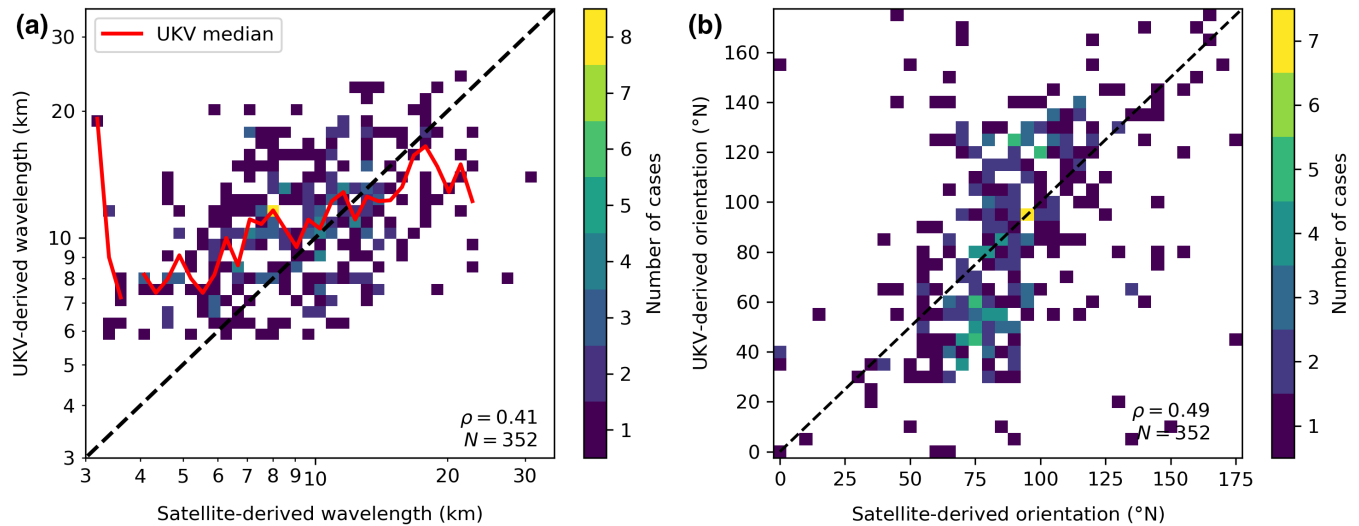
FIGURE 10   As in Figure 9, but for five-day lead time UKV forecasts. [Colour figure can be viewed at wileyonlinelibrary.com]

hour of the day, exact 48- and 120-hour lead-time forecasts were not available for all cases identified. To be able to retain all identified cases in further analysis, the lead time of the "two-day" forecasts was allowed to range from 42 to 48 hours and that of the "five-day" forecasts from 108 to 120 hours.

There is some variation in the number of detected wavevectors, with 1997 and 2093 for the two- and five-day forecasts, respectively (compared with 2049 for the analyses). Wavevectors were detected in 100% of cases at both lead times. There is thus no evidence of a decline in the model's ability to produce trapped lee waves with increasing lead time out to five days. However, Figure 9, displaying the case-by-case comparisons between the satellite imagery and the forecast data, shows that accuracy in the prediction of wave characteristics is lost with increasing lead time. For the two-day forecasts, a slight decrease in correlations in both wavelength and orientation is observed, but the model still appears skilful ($\rho = 0.61$ and 0.63, respectively). Correlations decrease significantly for the five-day forecasts ($\rho = 0.41$ and 0.49, respectively, Figure 10), although a positive trend remains. The decrease in correlation is not as severe in orientation as it is in wavelength, presumably because the possible wave orientations are largely determined by wind direction, which may be easier to forecast than the flow parameters that determine wavelength.

5 | CONCLUSIONS

A 2D wavelet transform technique was used for satellite-based evaluation of the wavelength and orientation of trapped lee waves produced by the convection-permitting UKV model and applied to data

from 2023. The technique was applied to model analyses of vertical velocity and to visible-channel geostationary satellite images, thus allowing for comparison between the two. Satellite imagery often contains many different cloud formations, so, to limit the number of undesired signals entering further analysis, the satellite images were pre-selected by eye to contain trapped lee-wave cloud signatures, and the wave signals subsequently extracted were required to be of sufficient amplitude and to be orientated within 50° of the local wind direction. This somewhat selective filtering of the data came at a cost: around 25% of images were deemed not to contain sufficiently clear trapped lee-wave signatures. Although the procedure for the estimation of wave characteristics was applied exclusively to visible satellite imagery of the UKV domain, it has the potential to be applied to any other available imagery, such as infrared imagery or imagery of other regions of the world.

The algorithm detected trapped lee-wave signals in the corresponding UKV data in all but one of the pre-selected cases, which is consistent with the high true positive rates found previously (Vosper et al., 2013). Because the absence of cloud signatures does not necessarily imply the absence of wave activity, the model's false-positive rate cannot be obtained through satellite imagery. However, an indication of the false-positive rate could be obtained by finding positive cases in the model data (e.g., using the deep learning algorithm developed by Coney et al. (2023)) and applying the algorithm developed here to the corresponding satellite images, wherever these contain visible wave signatures. It is likely that a more sophisticated algorithm would be required for such a procedure, as the one developed here has not been tested on images that do not contain trapped lee-wave signatures.

On average, the UKV model produced longer wavelengths than were present in the satellite imagery, with

the mean wavelengths being 10.7 km (at 800 hPa) and 9 km, respectively. At least part of this discrepancy is due to the UKV's inability to produce wavelengths below ~ 6 km ($\sim$ four times the grid spacing). The vertical velocities were analysed at the 800-, 700-, and 600-hPa levels. Whereas previous studies have used the 700-hPa level, here the highest number of trapped lee-wave signals was found at 800 hPa. Furthermore, the distribution of wavelengths at that level followed that derived from the satellite imagery most closely, suggesting trapped lee-wave cloud bands most commonly form closer to 800 hPa.

Wavelengths were also compared on a case-by-case basis. Large spreads in wavelengths and orientations were observed within single cases, so, to simplify the comparison between the model and satellite data, only the most prevalent wavevectors (i.e., combinations of wavelength and orientations) from each data source were compared for each case. These comparisons confirmed the frequent overestimation of wavelengths by the model and revealed that this bias is present particularly at short wavelengths (mean overestimation of 46% below 9 km, that is, $\sim$ six times the grid spacing). Weakening of the overestimation as wavelength increases suggests that the limited horizontal resolution of the UKV is the cause, but a larger number of cases with $\lambda \gtrsim 15$ km would be needed to confirm this. Despite the overestimation of short wavelengths and the difficulty in comparing wave characteristics case-by-case, the satellite and model-derived wavelengths are found to be correlated ($\rho = 0.67$).

The evaluation of trapped lee-wave orientations proved more difficult than that of wavelengths. The bias in satellite imagery towards zonally oriented wavevectors is likely a result of the high viewing angle of the satellite towards the UKV domain, which worsens the instrument's resolution significantly in the meridional direction. Zonally oriented wavevectors are thus resolved more easily by the instrument than meridionally oriented wavevectors, particularly at shorter wavelengths. A comparison with an image from a polar-orbiting satellite supports this hypothesis. On average, lee waves were found to be turned anticlockwise with respect to the wind direction, in both the satellite imagery and model data (by 2.8° and 2.4°, respectively).

Application of the wavelet transform technique to two- and five-day forecast data demonstrated that the model's ability to produce trapped lee waves is not limited to its analyses and that the model retains a large amount of skill in the prediction of wave characteristics at a two-day lead time. At a five-day lead time, correlations decreased considerably ($\rho = 0.41$ in wavelength), indicating a loss in skill, but the algorithm still detected a 100% true positive rate.

The high correlations found in the case-by-case comparisons of wavelength and orientation, together with the model's high true positive rate, imply that the model is skilful in producing the relevant atmospheric conditions for trapped lee-wave generation, particularly as the characteristics of trapped lee waves are highly sensitive to the flow parameters. An evaluation of wave amplitudes produced by the model, in addition to wavelengths and orientations, would certainly complement this work's findings, but was not possible here due to the scarcity of measurements of trapped lee-wave amplitudes.

The model's skill in producing wave characteristics is especially valuable given the lack of in situ measurements of trapped lee waves. It validates further the findings of previous model-based studies and climatologies of trapped lee waves and supports future model-based research into the conditions that generate the waves. A thorough understanding of these conditions is a necessary, but currently missing, step in the development of a trapped lee-wave drag parametrisation. From this perspective, it is encouraging that the UKV model has been shown to contain the information that is necessary to reproduce wave characteristics accurately. If a trapped lee-wave drag parametrisation is to be applied in larger-scale models, such as the global configuration of the MetUM that drives the UKV, such information will need to be available and accurate.

CONFLICT OF INTEREST STATEMENT
The authors declare no conflict of interest.

DATA AVAILABILITY STATEMENT
The UKV data were obtained from the Met Office Managed Archive Storage System (MASS) through JASMIN. The SEVIRI data were obtained via the EUMETSAT Data Access Client and the MODIS imagery via NASA's LAADS DAAC. The list of trapped lee-wave cases identified by eye from the SEVIRI imagery is available on Zenodo Houtman (2024). The code for characterisation of trapped lee waves from UKV and SEVIRI data is available at https://github.com/HetteHoutman.

ORCID
Hette G. Houtman https://orcid.org/0009-0007-5957-5756
Miguel A. C. Teixeira https://orcid.org/0000-0003-1205-3233

Suzanne L. Gray https://orcid.org/0000-0001-8658
-362X

Peter Sheridan https://orcid.org/0000-0002-0408-1501

Simon Vosper https://orcid.org/0000-0002-1117-4351

REFERENCES

American Meteorological Society. (2024) Mountain Wave. https://glossary.ametsoc.org/wiki/Mountain.wave

Bretherton, F.P. (1969) Momentum transport by gravity waves. *Quarterly Journal of the Royal Meteorological Society*, 95, 213–243.

Chen, C. & Chu, X. (2017) Two-dimensional Morlet wavelet transform and its application to wave recognition methodology of automatically extracting two-dimensional wave packets from lidar observations in Antarctica. *Journal of Atmospheric and Solar-Terrestrial Physics*, 162, 28–47.

Coney, J., Denby, L., Ross, A.N., Wang, H., Vosper, S., van Niekerk, A. et al. (2023) Identifying and characterising trapped lee waves using deep learning techniques. *Quarterly Journal of the Royal Meteorological Society*, 150, 213–231.

Coney, J., Ross, A., Denby, L., Wang, H., Vosper, S., van Niekerk, A. et al. (2024) A climatology of trapped lee waves over Britain and Ireland obtained using deep learning on high resolution model output (preprint). *Quarterly Journal of the Royal Meteorological Society*.

Fritts, D.C. & Alexander, M.J. (2003) Gravity wave dynamics and effects in the middle atmosphere. *Reviews of Geophysics*, 41, 1003.

Georgelin, M. & Lott, F. (2001) On the transfer of momentum by trapped lee waves: case of the iop 3 of pyrex. *Journal of the Atmospheric Sciences*, 58, 3563–3580.

Grubišić, V. & Billings, B.J. (2008) Climatology of the Sierra Nevada Mountain-wave events. *Monthly Weather Review*, 136, 757–768.

Hindley, N.P., Smith, N.D., Wright, C.J., Rees, D.A.S. & Mitchell, N.J. (2016) A two-dimensional Stockwell transform for gravity wave analysis of AIRS measurements. *Atmospheric Measurement Techniques*, 9, 2545–2565.

Hindley, N.P., Wright, C.J., Smith, N.D. & Mitchell, N.J. (2015) The southern stratospheric gravity wave hot spot: Individual waves and their momentum fluxes measured by COSMIC GPS-RO. *Atmospheric Chemistry and Physics*, 15, 7797–7818.

Houtman, H.G. (2024) Satellite-derived trapped lee wave activity over the UK and Ireland in 2023. https://zenodo.org/doi/10.5281/zenodo.13306650

Kim, Y.J. & Doyle, J.D. (2005) Extension of an orographic-drag parametrization scheme to incorporate orographic anisotropy and flow blocking. *Quarterly Journal of the Royal Meteorological Society*, 131, 1893–1921.

Lott, F. & Miller, M.J. (1997) A new subgrid-scale orographic drag parametrization: its formulation and testing. *Quarterly Journal of the Royal Meteorological Society*, 123, 101–127.

McFarlane, N.A. (1987) The effect of Orographically excited gravity wave drag on the general circulation of the lower stratosphere and troposphere. *Journal of the Atmospheric Sciences*, 44, 1775–1800.

Meyers, S.D., Kelly, B.G. & O'Brien, J.J. (1993) An introduction to wavelet analysis in oceanography and meteorology: With application to the dispersion of Yanai waves. *Monthly Weather Review*, 121, 2858–2866.

MODIS Science Team. (2017) MYD02QKM MODIS/Aqua Calibrated Radiances 5-Min L1B Swath 250m.

Nappo, C.J. (2012) *An Introduction to Atmospheric Gravity Waves*, 2nd edition. Oxford: Academic Press.

Saunders, R., Hocking, J., Turner, E., Rayer, P., Rundle, D., Brunel, P. et al. (2018) An update on the RTTOV fast radiative transfer model (currently at version 12). *Geoscientific Model Development*, 11, 2717–2737.

Schmetz, J., Pili, P., Tjemkes, S., Just, D., Kerkmann, J., Rota, S. et al. (2002) Supplement to an introduction to Meteosat second generation (MSG). *Bulletin of the American Meteorological Society*, 83, 992.

Scorer, R. (1949) Theory of waves in the lee of mountains. *Quarterly Journal of the Royal Meteorological Society*, 75, 41–56.

Sheridan, P., Vosper, S. & Brown, P. (2017) Mountain waves in high resolution forecast models: automated diagnostics of wave severity and impact on surface winds. *Atmosphere*, 8, 24.

Sheridan, P.F., Horlacher, V., Rooney, G.G., Hignett, P., Mobbs, S.D. & Vosper, S.B. (2007) Influence of lee waves on the near-surface flow downwind of the Pennines. *Quarterly Journal of the Royal Meteorological Society*, 133, 1353–1369.

Smith, R.B., Doyle, J.D., Jiang, Q. & Smith, S.A. (2007) Alpine gravity waves: lessons from map regarding mountain wave generation and breaking. *Quarterly Journal of the Royal Meteorological Society*, 133, 917–936. Available from: https://onlinelibrary.wiley.com/doi/full/10.1002/qj.103

Steeneveld, G.J., Holstag, A.A., Nappo, C.J., van de Wiel, B.J. & Mahrt, L. (2008) Exploring the possible role of small-scale terrain drag on stable boundary layers over land. *Journal of Applied Meteorology and Climatology*, 47, 2518–2530.

Stiperski, I. & Grubišić, V. (2011) Trapped lee wave interference in the presence of surface friction. *Journal of the Atmospheric Sciences*, 68, 918–936.

Tang, Y., Lean, H.W. & Bornemann, J. (2013) The benefits of the met Office variable resolution NWP model for forecasting convection. *Meteorological Applications*, 20, 417–426.

Teixeira, M.A. & Argaín, J.L. (2022) The drag exerted by weakly dissipative trapped lee waves on the atmosphere: application to Scorer's two-layer model. *Quarterly Journal of the Royal Meteorological Society*, 148, 3211–3230.

Teixeira, M.A., Argaín, J.L. & Miranda, P.M. (2013a) Orographic drag associated with lee waves trapped at an inversion. *Journal of the Atmospheric Sciences*, 70, 2930–2947.

Teixeira, M.A., Paci, A. & Belleudy, A. (2017) Drag produced by waves trapped at a density Interface in nonhydrostatic flow over an Axisymmetric Hill. *Journal of the Atmospheric Sciences*, 74, 1839–1857.

Teixeira, M.A.C., Argaín, J.L. & Miranda, P.M. (2013b) Drag produced by trapped lee waves and propagating mountain waves in a two-layer atmosphere. *Quarterly Journal of the Royal Meteorological Society*, 139, 964–981.

Torrence, C. & Compo, G.P. (1998) A practical guide to wavelet analysis. *Bulletin of the American Meteorological Society*, 79, 61–78.

Vosper, S.B., Wells, H., Sinclair, J.A. & Sheridan, P.F. (2013) A climatology of lee waves over the UK derived from model forecasts. *Meteorological Applications*, 20, 466–481.

Wang, N. & Lu, C. (2010) Two-dimensional continuous wavelet analysis and its application to meteorological data. *Journal of Atmospheric and Oceanic Technology*, 27, 652–666.

Xu, X., Li, R., Teixeira, M.A. & Lu, Y. (2021) On the momentum flux of vertically propagating orographic gravity waves excited in non-hydrostatic flow over three-dimensional orography. *Journal of the Atmospheric Sciences*, 78, 1807–1822.